Nanoscale Advances

ROYAL SOCIETY OF CHEMISTRY

PAPER

View Article Online
View Journal | View Issue

Cite this: *Nanoscale Adv.*, 2023, **5**, 5907

Impact of nitrogen doping on triazole-based graphitic carbon Nitride-TiO_2 (P25) S-scheme heterojunction for improved photocatalytic hydrogen production†

Saravanan Kamalakannan,[a] Natarajan Balasubramaniyan, *[a] Neppolian Bernaurdshaw[b] and Ganesh Vattikondala[c]

Establishing an S-scheme heterojunction is a promising method for increasing the photocatalytic activity of synthetic materials. In this study, nitrogen-doped g-C_3N_5/TiO_2 S-scheme photocatalysts have been synthesized and examined for photocatalytic hydrogen production using thermal decomposition methods. Nitrogen-doped g-C_3N_5/TiO_2 composites performed better than pure nitrogen-doped g-C_3N_5 and TiO_2 alone. Using experiments and density functional theory (DFT) calculations, nitrogen (N) doping was identified as being introduced by replacing the carbon (C) atoms in the matrix of g-C_3N_5. In addition to its narrow band gap, N-doped g-C_3N_5 showed efficient carrier separation and charge transfer, resulting in the enhanced absorption of visible light and photocatalytic activity. DFT, XPS, optical property characteristics, and PL spectra confirmed these findings, which were attributed to the successful nitrogen doping, and the composite was proven to be a potential candidate for photocatalytic hydrogen generation under light irradiation. The quantity of H_2 produced from the nitrogen-doped g-C_3N_5/TiO_2 composite for 3 hours (3515.1 μmol g^{-1}) was about three times that of N-doped g-C_3N_5. The H_2 production percentage of the nitrogen-doped g-C_3N_5/TiO_2 catalyst with Pt as the cocatalyst was improved by nearly ten times as compared to N-doped g-C_3N_5/TiO_2 without a cocatalyst. Herein, we report the successful preparation of the N-doped g-C_3N_5/TiO_2 S-scheme heterojunction and highlight a simple and efficient catalyst for energy storage requirements and environmental monitoring.

Received 4th August 2023
Accepted 22nd September 2023

DOI: 10.1039/d3na00597f

rsc.li/nanoscale-advances

1. Introduction

Researchers are interested in graphitic carbon nitride (CN) due to its exclusive properties, such as its non-metallic nature, thermal stability, chemical stability, governable semiconducting properties with the band gap energy of approximately 2.72 eV, small charge, ease of research, and eco-friendliness.[1,2] CN materials with C/N ratios ranging from 0.4 to 3 have been designated as C_3N_7, C_3N_6, C_3N_5, C_3N_4, C_3N_3, C_3N_2, C_3N, and so on. C_3N_x ($x = 1$–7) materials with various C/N ratios have been reported, with g-C_3N_4 being the most researched form of CN and receiving much attention over the past 20 years.[3,4] As a lone pair electron donor, N can enhance charge transfer and thus activate the photocatalytic performance; the sp^2-hybridized C and N for the triazine rings of g-C_3N_4 and the production of its C/N ratio play a vital role in the photocatalytic activity.[5] To the best of our knowledge, adding nitrogen to the carbon matrix of CNs results in a narrow band gap. It improves the field emission, photocatalysis, fundamental catalysis, carbon capture, electrical characteristics, and hydrogen production.[6,7] The primary focus of current research on CNs is the synthesis and description of their polymorphs. Unfortunately, these shapeless CN materials have limited long-term applications despite their exceptional nonporousness and small surface area.[8] In general, the H_2 generation rate during photocatalysis is insufficient for the light absorption capacity and poor quantum efficiency imposed by the charge carrier lifetime and low surface area.[9,10] As a result, enormous efforts were made to develop more reasonable model schemes suitable for visible-light photocatalysis.[11] Recently, several photocatalysts with various shapes and structures have been considered and synthesized. Due to its appropriate band size, physicochemical consistency, and other properties, the metal

[a]Department of Chemistry, SRM Institute of Science and Technology, Kattankulathur – 603 203, Tamil Nadu, India. E-mail: natarajb@srmist.edu.in
[b]Department of Chemistry, SRM Institute of Science and Technology, Kattankulathur 603 203, Tamil Nadu, India
[c]Department of Physics and Nanotechnology, SRM Institute of Science and Technology, Kattankulathur, 603203, Tamil Nadu, India

† Electronic supplementary information (ESI) available: XRD patterns, FT-IR spectra, TEM images, XPS survey spectrum of NCN, TiO_2, and $NCNT_5$ samples, pristine g-CN (g-C_3N_5), UV-vis spectra of g-C_3N_4, g-CN (g-C_3N_5), NCN (nitrogen-doped g-C_3N_5), and density functional theory (DFT) calculations. See DOI: https://doi.org/10.1039/d3na00597f

oxide semiconductor has attracted significant attention for photocatalytic hydrogen production.[12] Recently, alternate N-rich precursors, such as melamine, thiourea and urea have been used to expand the photocatalytic performance of CN materials. It is, therefore, critical to investigate N-rich CN materials with a unique low band gap and structure to improve photocatalytic performance. Varied forbidden gap energies and rapid recombination ratios of visible-light photo-induced (e^-/h^+) during photoexcitation have limited the photoactivity of generally considered photocatalyst materials such as SnO_2, WO_3, ZnO, and TiO_2.[13,14]

Recently, a high (N ratio) polymer CN material of C_3N_5 was reported for its excellent photocatalytic H_2 and organic pollutant degradation with a shorter band gap (2.20 eV) and larger conductive band CB potential (1.47 V) than the popular g-C_3N_4. However, as with other semiconductors, the consumption of photo-generated carriers by internal recombination limits its applications. Intriguingly, the band gap of g-C_3N_5 can be tuned between 1.7 and 2.0 eV to increase the visible-light reactive photocatalytic energies, which are smaller than that of g-C_3N_4 (2.7 eV).[15–17] Regarding structural engineering, many studies have found that g-C_3N_4 and g-C_3N_5, mesoporous construction, rod, and nanosheet-like formations have photocatalytic potential. The new material with a high N content has an extensive band gap range.[18] Though the prepared g-C_3N_5 outperforms some previously reported g-C_3N_4, the heavy templating process for preparing g-C_3N_5 is expensive and time-consuming. $CeTi_2O_6$,[19] a titanate photocatalyst material with a short band gap value of 2.73 eV, has been demonstrated to be advantageous in aggressive ionic conductors and semiconductor photocatalysts.[20,21] TiO_2 is the most commonly used photocatalyst in photocatalytic processes, and the application study shows its efficacy in photocatalytic hydrogen production. Essential aspects of this phenomenon include its low activity and broad band gap (3.24 eV) and its recyclability under light due to the high probability of photo-induced (e^-/h^+) recombination.

To prepare N-doped g-C_3N_5/TiO_2 S-scheme heterojunction catalysts, we used a one-step polymerization route with citric acid, 3-amino-1,2,4-triazole (3-AT), and TiO_2 (P25) as initial products this work.[22,23] Compared to g-C_3N_5 and TiO_2 (P25), a photocatalyst with a direct S-scheme heterojunction and an improved structure in N-doped g-C_3N_5/TiO_2, they exhibited increased interaction and toughness in visible light photocatalytic hydrogen production. Through three carboxyl groups, citric acid, a weak organic acid, remains among the most used predecessors in dehydration and carbonization reactions.[24,25] Because of its excellent properties and significant assets,[26] nitrogen N doping has attracted increasing interest. Advantages of N-doping include: (1) g-C_3N_5 electronic band structure regulation, (2) avoiding the drawbacks of foreign atom introduction, (3) g-C_3N_5 aromatic pi-conjugated system extended and delocalized,[27,28] (4) causing bordering carbon atoms to act equally as electron acceptors and electron donors. Nevertheless, N-doping of C_3N_5 is rarely used in photocatalytic hydrogen production applications.[29–31] This paper investigates the photocatalytic activity of N-doped g-C_3N_5/TiO_2 for hydrogen production. The chemical structure, optical absorption, shape, doping structure, and charge division have all been thoroughly investigated.[32] Because of the introduction of the N element, N-doped g-C_3N_5 has a slight band gap and efficient charge separation.[33] Under visible light, the obtained composites demonstrated significantly improved photocatalytic efficiency for hydrogen evolution by H_2O splitting.[34,35]

To the best of our knowledge, no extensive study has been directed toward preparing N-doped g-C_3N_5/TiO_2 S-scheme heterojunction composites and their application in photocatalytic hydrogen production. The photocatalytic appearances of the NCN/TiO_2 obtained were significantly improved. This study's N-doped triazole-based g-C_3N_5 opens the door to the growth of a novel CN-based material for photocatalytic hydrogen production with a wide range of applications. In this study, N-doped g-C_3N_5 (NCN) with nitrogen doping demonstrated significantly higher photocatalytic activity than new g-C_3N_5. When elemental nitrogen was added to g-C_3N_5, its increasing light absorption capacity resulted in many more photosensitive charge carriers. Additionally, surface impurities aided in the separation of (e^-/h^+) pairs. Exciting new materials could be achieved with n-doping and S-scheme heterojunctions to produce NCN/TiO_2 photocatalysts. As a result, developing an N-doped g-C_3N_5 sheet structure using a single-pot method was significant. We hope that the novel class of N-doped g-C_3N_5/TiO_2 composite nanomaterials are among the best candidates in hydrogen production applications.

Herein, we synthesized N-doped g-C_3N_5/TiO_2 nanocomposites using a citric acid monohydrate and 3-amino-1,2,4-triazole (3-AT) to prepare a series of g-C_3N_5/TiO_2 photocatalysts with N doping and evaluated the performance of photocatalytic H_2 production. 3-AT decomposed at high temperatures to yield cyanamide and hydrazoic acid, which also reacted with citric acid to produce a carbon nitride monomer containing two triazines and one triazole unit. Then, the N-doped triazole-based g-C_3N_5/TiO_2 was synthesized *via* a polycondensation reaction with the elimination of NH_3 at 550 °C. Scheme 1 represents the formation of an N-doped triazole-based g-C_3N_5/TiO_2 S-scheme heterojunction using citric acid monohydrate, TiO_2 (P25), and 3-AT as precursors.

2. Experimental section

2.1. Synthesis of bulk g-C_3N_5

The bulk g-C_3N_5 nanosheet was derived as follows: 5 grams of 3-amino-1,2,4-triazole was ground and then heated to (550 °C) for 3 hours at a ramp rate of 5 °C per minute. After subsequent cooling, the product was obtained and ground for characterization and applications. Comparatively, g-C_3N_4 was prepared through two sessions of calcination at 550 °C for three hours with intermediate grinding using melamine as the starting material. The triazole-based g-C_3N_5 produced only by 3-AT was designated as g-CN.

2.2. Synthesis of nitrogen-doped g-C_3N_5

A mixture of 5 grams of 3-amino-1,2,4-triazole (3-AT) powder and 5 mg of citric acid monohydrate was ground, then heated to

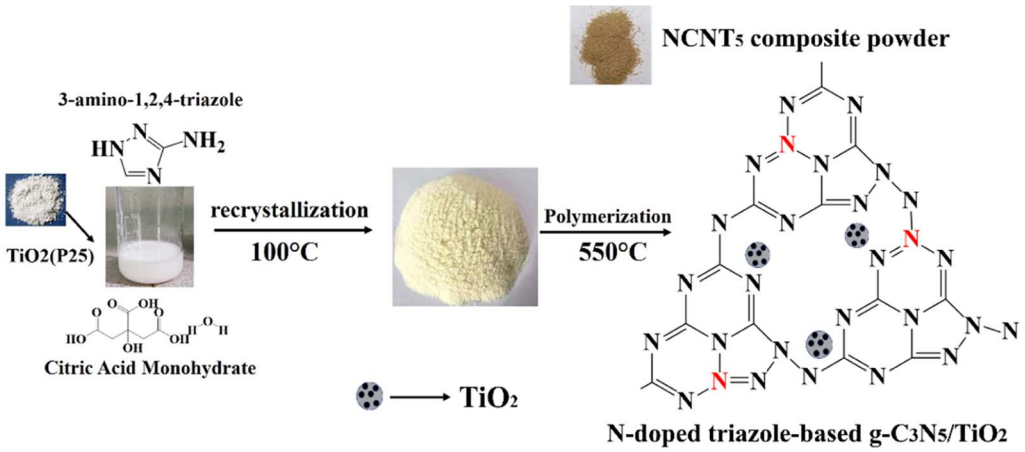

Scheme 1 The construction of the $NCNT_x$ S-scheme heterojunction photocatalyst.

550 °C for 3 hours at a ramp rate of 5 °C min^{-1}. After cooling, the N-doped g-C_3N_5 was washed several times with deionized water and ethanol before being used for further experiments. NCN denotes the nitrogen-doped g-C_3N_5 produced by 3-AT and citric acid alone.

2.3. Preparation of nitrogen-doped g-C_3N_5/TiO_2 heterostructures

The following is a description of the NCN/TiO_2 formation process. The S-scheme heterojunction photocatalysts were prepared by dissolving variable amounts of 3-amino-1,2,4-triazole (3-AT) precursor (1, 2, 3, 4, and 5 g) and 5 mg of citric acid monohydrate in 50 mL of (DI) water to form a solution. A suspension was then formed by adding 0.2 g of TiO_2 (P25) to the solution with stirring. The suspensions were stirred for 2 hours before being dried by evaporation at 100 °C. To obtain the final NCN/TiO_2 composites, the samples were calcined at 550 °C for 3 hours at 5 °C min^{-1}. The products designated $NCNT_1$, $NCNT_2$, $NCNT_3$, $NCNT_4$, and $NCNT_5$.

2.4. Photocatalytic H_2-production

The photocatalytic H_2 production reaction was conducted in direct sunlight on the terrace of the SRM IST main block in the Kattankulathur Campus, Tamil Nadu, India. Here, 5 milligrams of composite catalyst was added to 50 mL of 5 volumes of aqueous triethanolamine solution in a 100 mL Pyrex reactor. Next, 3 wt% Pt as a precursor was added to the photocatalysis solution. By purging the reaction solution with nitrogen gas for 30 minutes, the dissolved O_2 was eliminated. The combined reactants were exposed to light, and the resulting hydrogen gas evolution was detected using gas chromatography (Shimadzu, GC-2014, Molecular Sieve/5 Å column) equipped with a TCD detector. The reactions were achieved between 10:50 a.m. and 1:50 p.m. to ensure the integrity of all experiments carried out in direct sunlight (IST). Solar light density was measured and recorded using a lux meter (TES1332A), and the typical light intensity was measured to be 1358.8 W m^{-2} in the summer and 790 W m^{-2} in the wintertime.

2.5. Photoelectrochemical analysis

The arranged photocatalysts' photoelectrochemical properties were investigated using a counter electrode (Pt), a reference electrode (Ag/AgCl), and a working electrode covered with the appropriate photocatalyst. In the procedure, 5 milligrams of catalyst were ultrasonically dispersed in a 1 : 1 water and ethanol mixture with 0.005 mL of Nafion. The mixture was added dropwise to the glassy carbon (GC) electrode, and the electrochemical study was carried out with the help of an electrochemical workstation (Biologic SP150). The electrolyte was maintained as a 0.1 M sodium sulfate solution. A solar simulator (1.5 AM) was used as the light source (SSEM, 300 W, Photo Emission Tech, USA).

2.6. Characterization studies

Using XRD (X-ray diffraction analysis) and Cu Kα radiation (=1.5406 A), the crystalline phase and crystallinity of the sample used to prepare the photocatalyst were ascertained. The PHI Versa Probe III XPS was used to perform the X-ray photoelectron spectroscopy (XPS). Testing was performed using a Shimadzu IRTracer-100 FT-IR spectrometer. Scanning electron microscopy (SEM, TFC, Apreo S) and Transmission electron microscopy were used to examine the sizes and shapes of the nanocomposites (TEM, JEOL Japan, and JEM-2100 Plus). The specific surface area and Barrett–Joyner–Halenda (BJH) pore size distribution were calculated using the Autosorb IQ from Brunauer–Emmett–Teller's (BET) Quantachrome Instruments. A UV-vis spectrophotometer was used to record UV-vis diffuse reflectance (UV-DRS) spectra (Shimadzu, UV-3600i Plus). The PL and (TRPL) spectra were analyzed with a fluorescence spectrophotometer (Horiba, Fluorolog-QM).

3. Results and discussion

3.1. Structure analysis

In this study, we prepared N-doped triazole-based g-C_3N_5/TiO_2 S-scheme photocatalysts using 3-AT, citric acid, and TiO_2 as raw materials. Using 3-AT resulted in the formation of a particular

N-rich CN pattern of triazole units, a substitute chemical for synthesizing CN with a larger N-content and low band energy.[36,37] Fig. 1a depicts the XRD patterns of $NCNT_x$ samples, showing all the significant diffraction peaks of produced TiO_2. TiO_2 (P25) diffraction peaks at 25.3, 36.9, 37.9, 38.5, 48.1, 53.9, 55.3, 62.5, 68.7, 70.5, and 75.2 correspond to plane values (1 0 1), (1 0 3), (0 0 4), (1 1 2), (2 0 0), (1 0 5), (2 1 1), (2 1 3), (1 1 6), (2 2 0), and (1 0 7), respectively. Fig. S1a† shows mainly two peaks at approximately 13° and 27°, corresponding to the graphitic carbon nitride planes (100) and (002). The peak allocated to the (002) plane of NCN has a greater 2θ value than that of the g-C_3N_4 spectrum, which is consistent with an earlier report[38] and confirms the formation of the NCN structure. The two triazine and triazole rings in the g-CN unit could be responsible for twisting the sheet structure and reducing the interlayer space in the (002) direction. The XRD patterns of $NCNT_x$ samples contain all of the NCN and TiO_2 peaks in Fig. 1a, which concurs with the findings from HRTEM images. Fig. 1b demonstrates that compared with bare g-CN, the XRD pattern of NCN showed no noticeable change, indicating that NCN retained its molecular structure. The peak frequencies of $NCNT_x$ were slightly shifted from TiO_2 (for example, on the (004) plane of anatase TiO_2 and the (110) plane of rutile TiO_2) due to the strong intrinsic interactions between TiO_2 and NCN_x. A close connection facilitated the transfer of charge carriers induced by photocatalysis.[39,40] This can be credited to the effective intrinsic interface between TiO_2 and NCN. The XRD patterns of g-C_3N_4, g-CN (g-C_3N_5), and NCN (N-doped g-C_3N_5) are shown in Fig. S1a.† The slight shift in the location of the NCN peaks from 27° to 27.6° indicated that the N element had been successfully doped into g-CN. This finding suggests that using too much citric acid may cause the production of undesired impurities during the synthesis of N-doped g-C_3N_5.

FTIR analysis was used to examine the fundamental components of $NCNT_x$ samples. Except for a few minor differences, the FTIR spectra of $NCNT_x$ samples revealed similar results in Fig. 1c. The absorption band at 466 cm^{-1} in the pristine TiO_2 spectrum is caused by the stretching vibrations of Ti–O–Ti and Ti–O in anatase crystals. According to FTIR analysis of the surface functional groups of these samples, the primary spectrum in the range of (1200–1600 cm^{-1}) could be attributed to the C–N/C=N heterocycles of the carbon nitride unit. Another peak was detected at 824 cm^{-1} for the triazine unit breathing vibration.[41] These peaks were observed to be

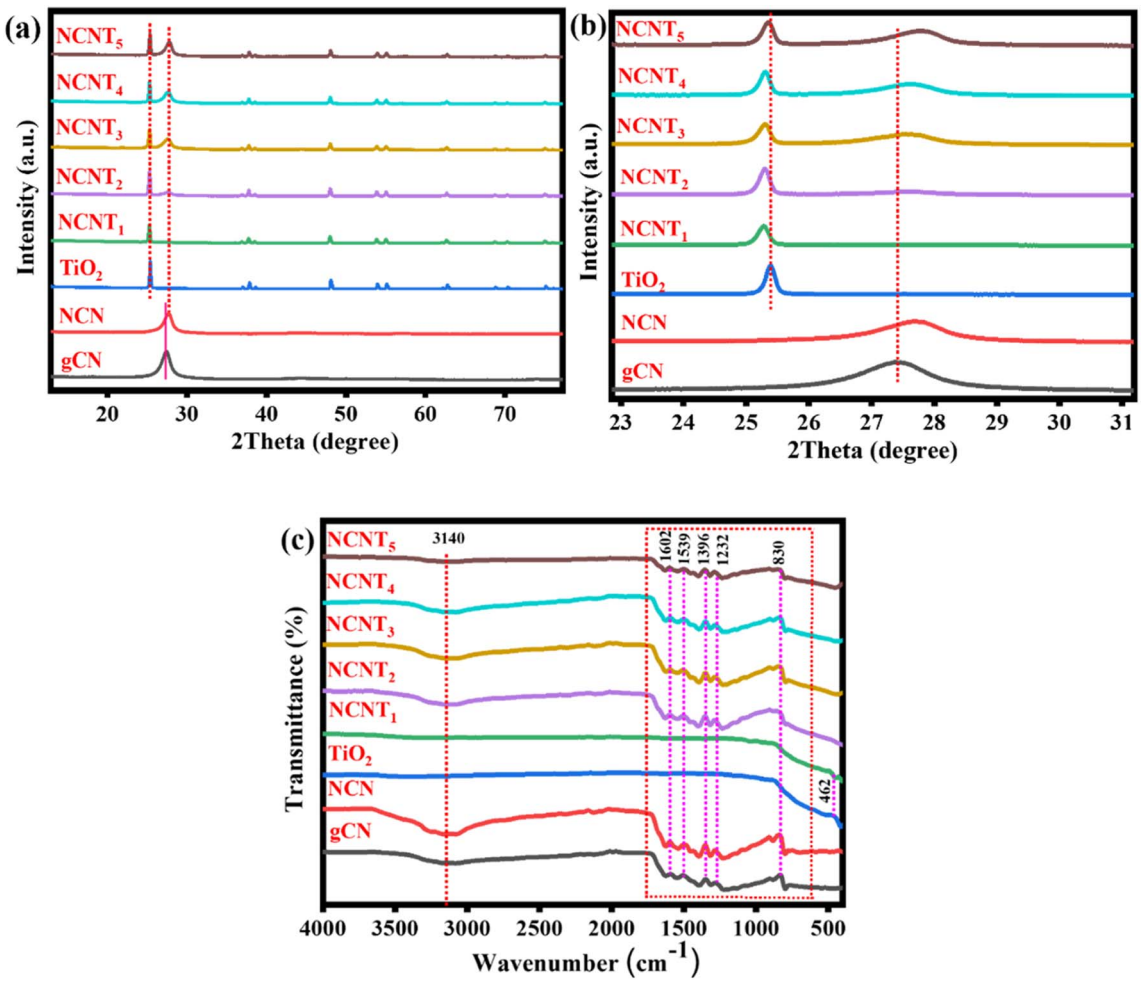

Fig. 1 XRD patterns (a and b) and FT-IR spectra of the (g-CN, NCN, TiO_2, and $NCNT_x$) (c).

attributed to N–N stretching (1270 cm^{-1}) in triazole-based moieties, and C–N (1334 cm^{-1}) and C=N (1594 cm^{-1}) in triazine units, including both. The peak at 3100 cm^{-1} was caused by the observed stretching vibrations increase of $-NH_2$ and –OH of adsorbed H_2O molecules.[42] Again, the H bond-like connection that gently shifted to a smaller wavenumber and extended peak as compared to NCN at around 1500 cm^{-1} could indicate the formation of protonated graphitic nanosheets.[43] Furthermore, the H_2 bond between –NH–/–NH_2 was broken after protonation, as proved by the expansion of the adsorption peaks of –NH– or –NH_2 groups in the FT-IR spectra at 3500 cm^{-1} to 3000 cm^{-1}.[44] Despite this, the XRD and FTIR results indicated that these samples were successfully formed and maintained the N-doped g-C_3N_5/TiO_2 structure. The FT-IR spectra of g-C_3N_4, g-CN, and NCN are shown in Fig. S1b.† It was discovered that there was no discernible difference between the FT-IR spectra of g-C_3N_4 and g-CN, NCN, indicating that NCN retained the molecular structure of g-CN. Nevertheless, XRD and FTIR findings indicated that the g-C_3N_5 structure was successfully formed and well preserved after N-doping in these samples.

3.2. Morphological characteristics

Fig. 2a–c depict SEM images of the structures and morphologies of bare g-CN, NCN, TiO_2, and $NCNT_x$ composites. Fig. S2a† clearly shows the rough carbon nitride g-CN sheet layered structure with irregular thickness.[45] Fig. 2a depicts the sheet-like structure of the nitrogen-doped carbon nitride NCN with a distinct thickness. In Fig. 2b, the TiO_2 sample displays polydisperse spherical morphologies with sizes ranging from 500 to 800 nm. The $NCNT_5$ composite, produced by heating a combination of 3-AT and TiO_2, retained the forms of TiO_2, as depicted in Fig. 2c. Surprisingly, the thermal polymerization SEM of 3-AT (NCN) exhibited a sheet-like appearance on the surface of the TiO_2, which was closely and uniformly coated. The EDX results of NCN and $NCNT_5$ in Table S1† show that the weight percentage of nitrogen increased, respectively. Table 2 shows EDX and XPS analysis results, which confirmed nitrogen enrichment in NCN and $NCNT_5$.

The surface morphology and structures of the g-CN, NCN, TiO_2, and $NCNT_x$ samples were studied using TEM images. As seen in Fig. 2d–f, all the pieces were made up of sheet-like spherical structures. Thermal decomposition and copolymerization can form g-CN (g-C_3N_5) nanosheets, as shown in Fig. S2c,† which are shorter and lighter than g-C_3N_4 nanosheets. Fig. S2d† reveals polydisperse spherical morphologies in the 200 nm region in the TiO_2 sample. By the edge of the sheet shape with N-doping content in Fig. 2d, a few nanosheets smaller than 200 nm were generated, resulting in a clear surface area of the g-CN sample. Even though the pieces were sonicated for 45 minutes prior to the TEM measurement, NCN was attached to TiO_2 in a spherical sheet-like manner Fig. 2e. Lattice folds with *d*-spacings of 0.351 nm and 0.246 nm, respectively, confirmed the (110) and (004) planes of the hexagonal structure seen in $NCNT_5$ in Fig. 2f. A distinct grain edge indicated that an S-scheme heterojunction layout was formed in the $NCNT_x$ composites. This further validated the structural stability of the $NCNT_5$ composite. Lattice spacings of 0.351 and 0.246 nm correspond to the (110, 004) planes of the rutile and anatase phases of TiO_2.[46,47]

3.3. Sample pore size analysis

N_2 adsorption analysis was also used to limit the textural assets of as-arranged samples. As depicted in Fig. 3a, type (IV) isotherms by H3 hysteresis curves at the comparative pressure series of 0.0 to 1.0 are present in the prepared samples' mesoporous formations. The (BJH) pore size circulation plots (inset) show mesoporous appearances, including the 2–200 nm primary pore size. As determined by BET, the surface areas of NCN, TiO_2, and $NCNT_5$ composites were 32.87, 74.68, and 115.35 $cm^3\ g^{-1}$, respectively. The $NCNT_5$ photocatalyst has a large surface area,[48] indicating that the recombination rate of photo-generated charge carriers remained low. The increased

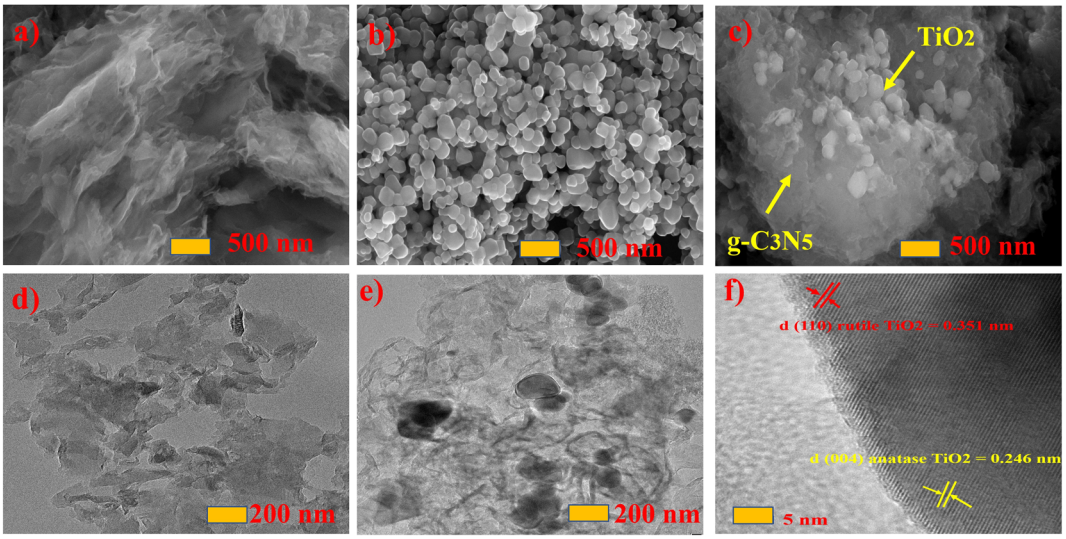

Fig. 2 SEM of the NCN, TiO_2, and $NCNT_5$ (a–c), and TEM of the NCN, $NCNT_5$, and fast Fourier transform FFT (d–f).

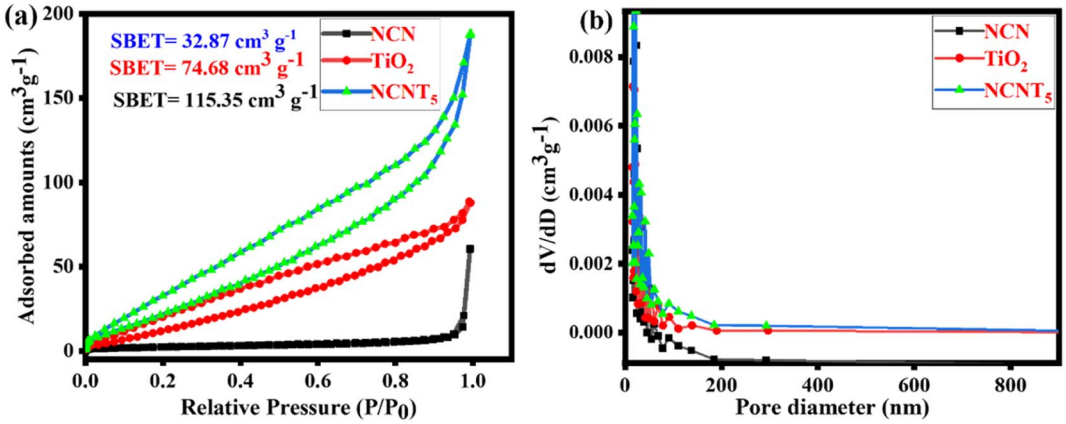

Fig. 3 N_2 adsorption/desorption isotherms (a) and pore size distribution of the NCN, TiO_2, and $NCNT_5$ samples (b).

diameter range, pore size, migration, and isolation of photo-generated carriers' optical properties all contributed to the increased photocatalytic activity. The $NCNT_5$ composite is advantageous for improved adsorption.[49,50] According to the findings above, it gives a more significant number of responsive positions for photocatalytic processes, significantly impacting the development of photocatalytic efficiency. TiO_2 and $NCNT_5$ samples have a larger specific surface area than pure NCN. Fig. 3b depicts the distribution of pore sizes. $NCNT_5$ has a broad pore size distribution curve of 8–200 nm, and its pore volume is (0.289 $cm^3\ g^{-1}$), which is two times that of TiO_2 (0.138 $cm^3\ g^{-1}$) and nearly three times that of NCN (0.105 $cm^3\ g^{-1}$). The BET surface area, pore volume, and pore size of all samples are shown in Table 1. TiO_2 and $NCNT_5$ samples have a larger specific surface area than pure NCN. The increased concentration of 3-amino-1,2,4-triazole in the final material may be responsible for the improved specific surface area of NCNT5.

3.4. Surface chemical composition (XPS)

The chemical valence states and surface elemental compositions of $NCNT_5$, NCN, and TiO_2 samples were confirmed using XPS analysis. XPS survey data confirmed that $NCNT_5$, NCN, and TiO_2 composites primarily contain the four elements (Ti, O and C, N) Fig. 4i. The two peaks positioned at (458.05/457.95 eV) and (464.08/463.97 eV) in the high-resolution Ti 2p spectra in Fig. 4a and g, are credited to (Ti $2p_{3/2}$) and (Ti $2p_{1/2}$), respectively,[51] indicating the occurrence of Ti^{4+} in TiO_2 and $NCNT_5$. Two chemical positions of O 1s for $NCNT_5$ and TiO_2 were found for the H–R O 1s spectra in Fig. 4b and h, at (529.15/529.37 eV) and (531.37/531.90 eV), which are attributed to O_2^--type and OH^- bonds. The peaks from NCN and $NCNT_5$ at (284.65/284.48 eV and (288.24/288.01 eV) in the C 1s H–R spectra in Fig. 4c and e can be a reason for the (C–N and N–C=N) bond groups.[52] The significant donation peak at (288.24 and 288.01) eV is attributable to the sp^2-hybridized C bonded to the nitrogen atom within the triazine rings. As shown in Fig. 4d and f, the H–R N 1s spectrum of $NCNT_5$ differs slightly from that of NCN. The N 1s spectrum of NCN and $NCNT_5$ can be separated into five peaks with binding energies of 398.1 eV, 398.9 eV, 399.7 eV, 400.2, 403.7 eV, and 397.5 eV, 398.2 eV, 399.2 eV, 400.1 eV, 402.3 eV, respectively. The dominant peaks at 398.1 and 397.5 eV are attributed to sp^2-hybridized nitrogen in C-containing triazine rings (C–N=C). In contrast, the peaks at 398.9 and 398.2 eV are usually attributed to tertiary N in N–$(C)_3$ groups.[53,54] The amino groups (C–N–H) are indicated by the peaks at 399.7 and 399.2 eV, while π excitation is indicated by the height at 403.7 and 402.3 eV. Another peak at 400.2 and 400.1 eV) corresponding to graphitic N, can be seen in samples NCN and $NCNT_5$, signifying that nitrogen-doped graphitic carbon has been created and is present in the g-C_3N_5 composite.[55,56] When citric acid was added to g-C_3N_5, N–N and N=N bond peaks appeared, indicating that nitrogen replaced the carbon atom. Notably, when TiO_2 is coupled with NCN, a slight peak change of Ti 2p, O 1s, C 1s, and N 1s is observed, which applies to the electron screening caused by the variation in electron density. The C–N, N–$(C)_3$, N–C=N, and C–N=C peaks revealed that the g-CN, NCN, and $NCNT_5$ structures are triazole/triazine unit hybrids (Table 2). The g-CN peaks at 284.70 and 288.64 eV in the C 1s high-resolution spectrum of Fig. 4j correspond to the C–N and N–C=N bond groups. The C–N=C and sp^3 N–$(C)_3$ bonds were attributed to two peaks at approximately 398.50 and 399.60 eV in the H–R N 1s spectra shown in Fig. 4k.[3,46] X-ray photoelectron spectroscopy and g-CN and NCN results all supported the idea that the g-C_3N_5 structure was successfully formed and well preserved in these samples before N-doping. In general, surface electron density is negatively related to binding energy.[57] The internal electric field (IEF) was formed when electrons transferred from NCN to TiO_2 after contact, as shown by the XPS results.

Table 1 Surface characteristics of prepared samples

Samples	S_{BET} ($cm^3\ g^{-1}$)	Pore volume ($cm^3\ g^{-1}$)	Pore size (nm)
NCN	32.87	0.105	14.30
TiO_2	74.680	0.138	16.23
$NCNT_5$	115.351	0.289	16.21

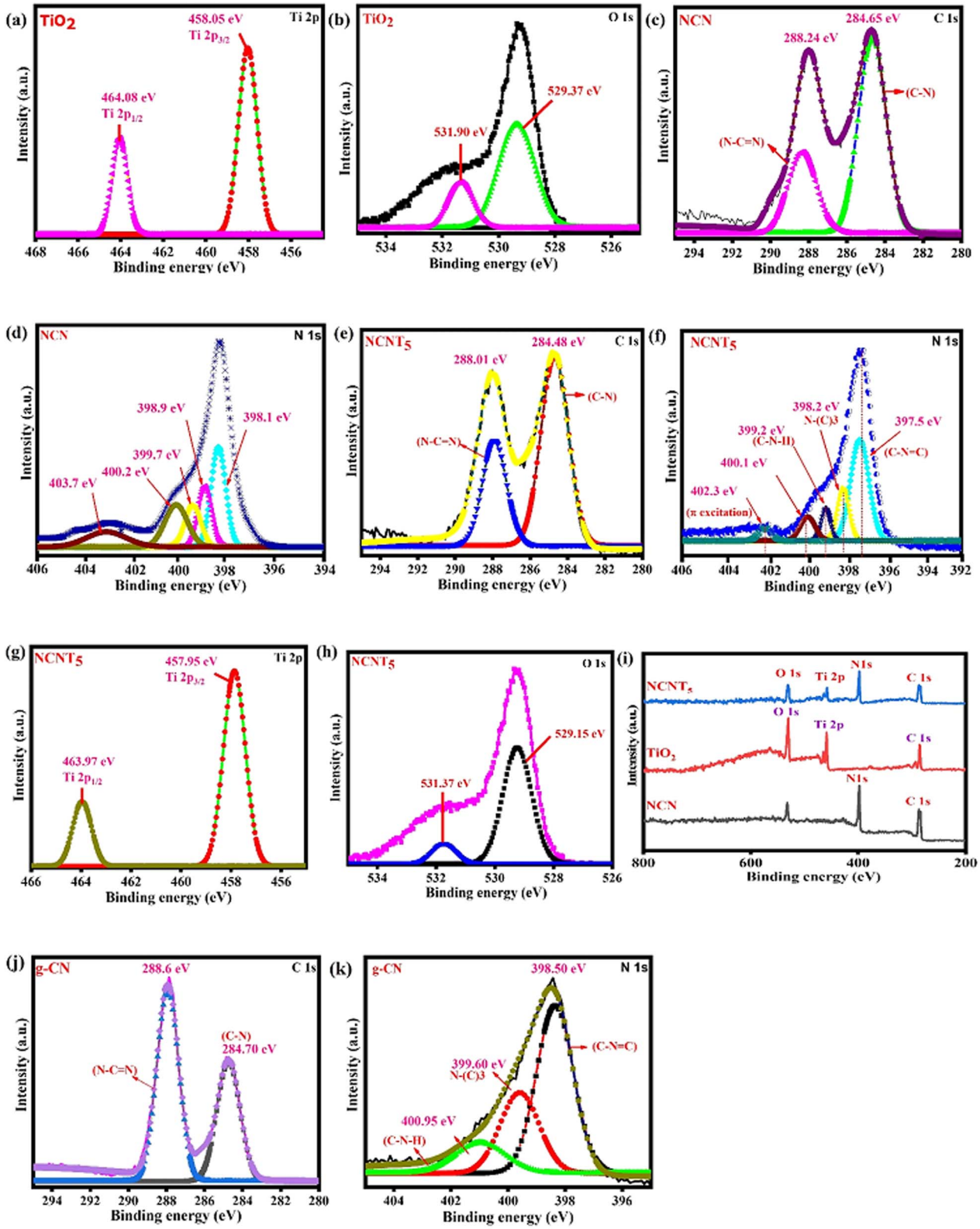

Fig. 4 XPS of (Ti 2p, O 1s) from TiO_2 (a and b), XPS of C 1s and N 1s from NCN (c and d), XPS of C 1s, N 1s, Ti 2p and O 1s from $NCNT_5$ (e–h), XPS survey spectra of NCN, TiO_2 and $NCNT_5$ samples (i), and pristine g-CN of C 1s, N 1s (j and k).

3.5. Energy band structure and photoelectric properties

UV-vis spectra were used to characterize the photocatalytic activity of g-CN, NCN, TiO_2, and $NCNT_x$, and the correlating DRS (diffuse reflectance spectra) were generated using the Kubelka–Munk method,[58] as shown in Fig. 5a and b. In the visible wavelength spectrum, 400–800 nm, the band gaps of the

Table 2 An analysis of deconvoluted XPS spectra revealed the binding energies and valence bond percentages for carbon and nitrogen

Samples	C–N	N–C=N	C–N=C	N–(C)$_3$	C–N–H
g-CN	37.61 (284.70)	62.39 (288.6)	53.25 (398.50)	29.11 (399.60)	17.51 (400.95)
NCN	29.82 (284.65)	70.18 (288.24)	44.67 (398.1)	30.84 (398.9)	24.47 (399.7)
NCNT$_5$	36.28 (284.48)	63.28 (288.01)	46.90 (397.5)	29.97 (398.2)	23.12 (399.2)

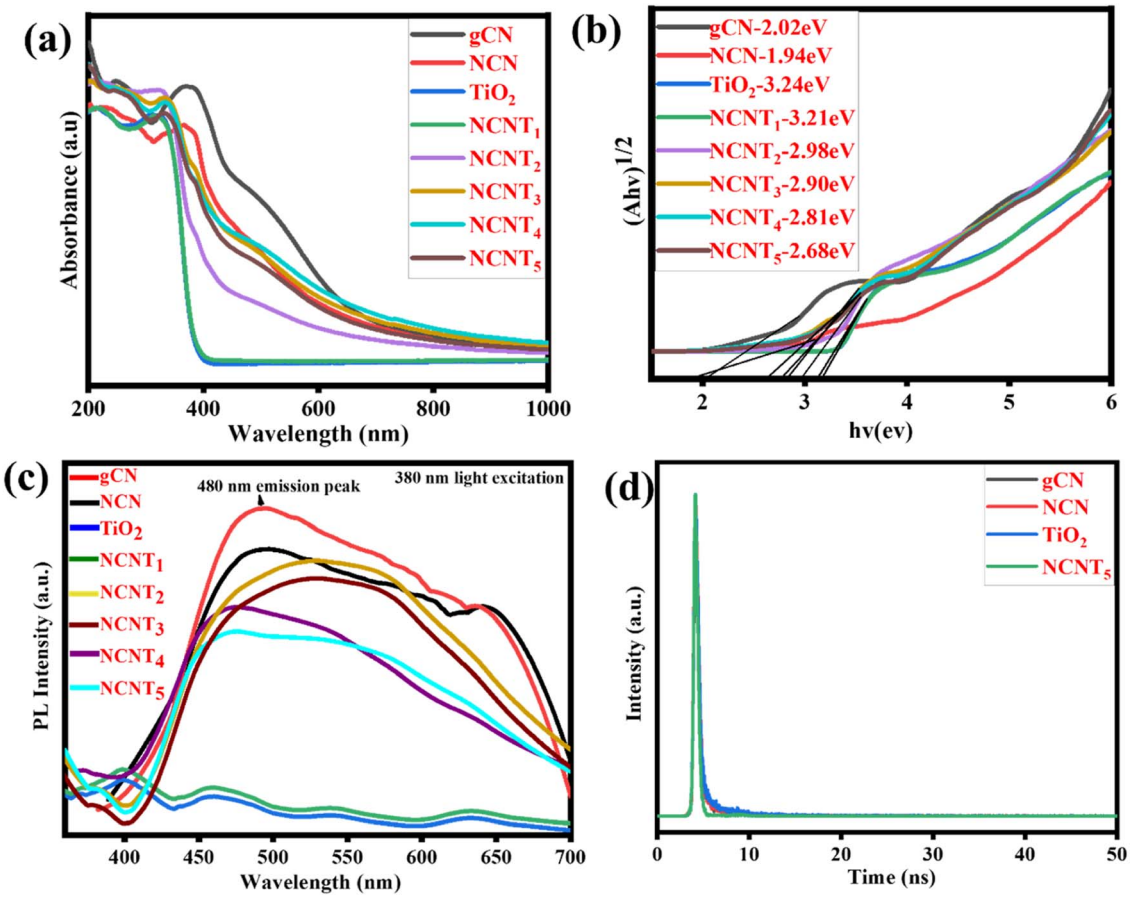

Fig. 5 UV-DRS spectra (a), plots of band gap (b), PL spectra of (g-CN, NCN, TiO_2, and NCNT$_x$) (c), time-resolved photoluminescence (TRPL) of bare g-CN, NCN, TiO_2, and NCNT$_5$ (d).

NCN and NCNT$_x$ were red-shifted and the spectral intensity was more significant than that of the g-CN, which may be attributed to the Nitrogen-doped photocatalysts' intrinsic regulation of the interactive band structure or the hierarchical system. The optical properties of the NCNT$_x$ samples were investigated using UV-vis photographs, as illustrated in Fig. 5a and the inset. As previously reported, TiO_2 exclusively shows the optical absorption of UV light.[59] The standard wide absorption bands of g-CN, NCN, and NCNT$_x$ were observed, relating to the raw band-to-band shift edges of absorbance at 461 to 666 nm, comparable to the optical properties shown in Fig. S3.† As a result, the E_g values of g-CN, NCN, TiO_2, and NCNT$_x$ were estimated to be 2.02, 1.94, 3.24, 3.21, 2.98, 2.90, 2.81, and 2.68 eV Fig. 5b. The higher visible-light spectrum of NCN in comparison to g-C_3N_5 suggested that NCN had more excellent illumination capability over a broader range of visible-light wavelengths. The correlation among the N 2p orbitals of the connecting azo-nitrogen of triazole-rings, the heptazine π-conjugated process,[60] which spans the π-conjugation network, is primarily responsible for the more extended absorption of C_3N_5. The increased visible light absorbance of NCNT$_x$ was related to the presence of nitrogen in carbon sites in the NCN unit. It can generate donor regions in the forbidden gap from its N 2p level and contribute too many electrons, thereby refining photocatalytic activity.[61] A UV-Vis spectrum of g-C_3N_4, g-CN, and NCN is shown in Fig. S3.† The energy gap of g-CN is higher than that of g-C_3N_4; after doping nitrogen in g-CN, the band gap was considerably reduced relative to the g-C_3N_4. The results showed that NCN and NCNT$_x$ have a smaller band gap than g-CN, which is helpful for light absorption and raises photocatalytic activity.[62]

Fig. 5c depicts the photoluminescence spectra of g-CN, NCN, TiO_2, and $NCNT_x$ composite samples under 380 nm light excitation. Similar to prior reports, neither TiO_2 nor $NCNT_1$ exhibited a detectable emission peak. Although the g-CN and NCN had the highest PL, the peak intensities of the $NCNT_2$ to $NCNT_5$ composites were significantly reduced after the NCN was attached to TiO_2. As for the low NCN in the composite,[63] the $NCNT_5$ sample showed no observable emission peaks. The other composites, on the other hand, displayed exceptional photoluminescence signals. Among the $NCNT_x$ ($x = 2$, 3, 4, and 5) samples, the $NCNT_5$ sample had low PL intensity, indicating that charge carrier recombination in the composite was critically restricted due to the S-scheme heterojunction structure at the interface of NCN and TiO_2. The overall characteristic peaks of these tests showed that the intensity of their PL emission was reduced following N-doping, with $NCNT_5$ exhibiting the average PL emission, *i.e.*, the average charge recombination of these samples.[64,65] An exciting suppression of (e^-/h^+) pair recombination may cause the hybrid to generate different photo-induced carriers, activating the photocatalytic reaction.

Time-resolved photoluminescence (TRPL) of bare g-CN, NCN, TiO_2, and $NCNT_5$ are shown in Fig. 5d, and Table S2† shows the results of a TRPL performed to estimate the lifetime of the charge carriers. The PL emission peak located at approximately 480 nm was determined. Further, bare g-CN, NCN, TiO_2, and $NCNT_5$ all had average lifetimes of 2.21, 1.98, 2.35, and 1.49 ns. The average charge carrier lifetime of $NCNT_5$ was 1.49 ns, which is significantly shorter than that of NCN (1.98 ns); this is related to the decreased recombination rate and longer charge carrier lifetime, and was confirmed by Nyquist plots and transient photocurrents.[66,67] The $NCNT_5$ heterojunction demonstrated the best charge-transfer efficiency based on the average lifetime of the four samples.

Fig. 6a depicts the cyclic photocurrent curves of pure NCN, TiO_2, and $NCNT_5$. When a light source is turned on and off, the photocurrent intensities sharply increase and decrease, indicating the formation of photo-induced electrons under visible irradiation. The transient photocurrent density is slightly higher in the $NCNT_5$ composite than in the NCN and TiO_2 systems, meaning that $NCNT_5$ can generate more electrons when exposed to visible light. This is stable with the significantly higher current density of the $NCNT_5$ sample when

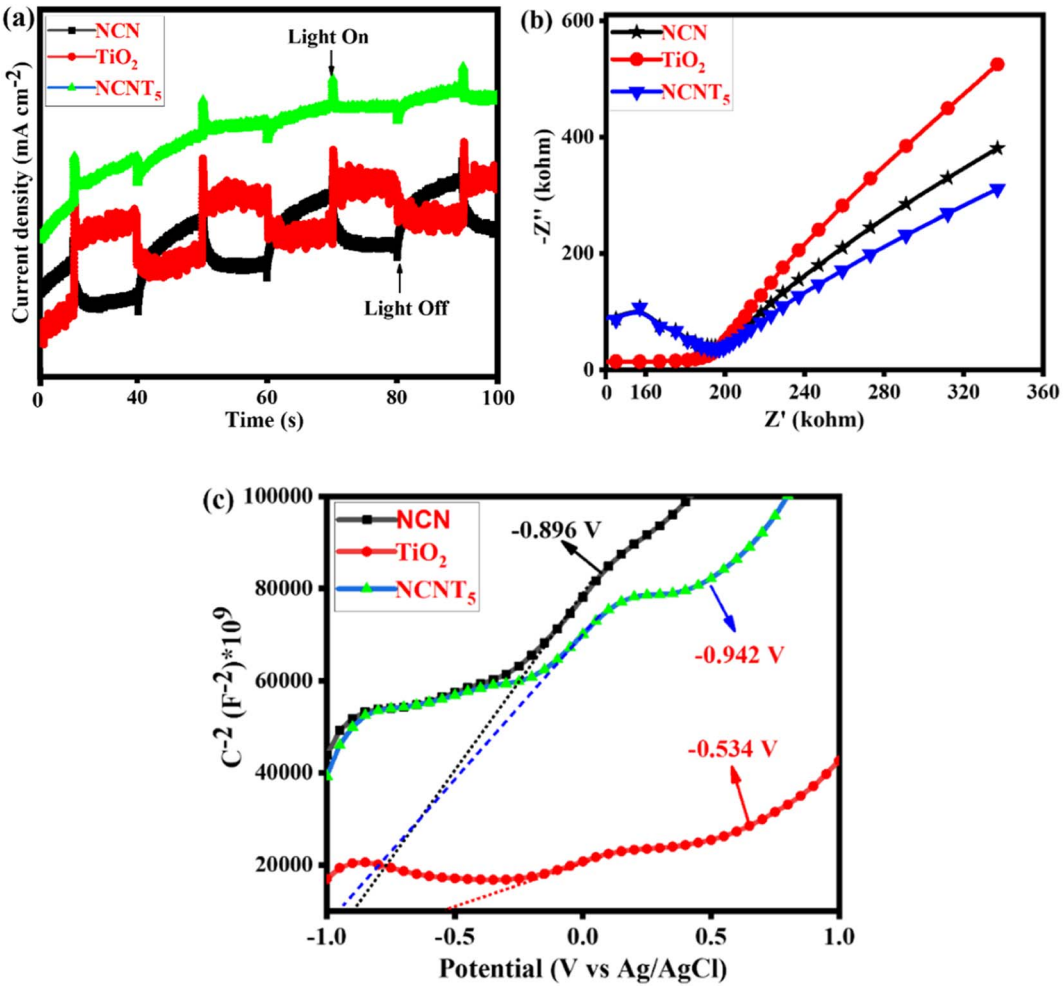

Fig. 6 Photocurrent spectra (a), Nyquist plot (b), and Mott–Schottky plots of NCN, TiO_2, and $NCNT_5$ samples (c).

Table 3 The band gap, valence band edge, and conduction band edge potentials of NCN, TiO_2, and $NCNT_5$ catalysts on a standard hydrogen electrode

Semiconductor	E_g (eV)	E_{CB} (eV)	E_{VB} (eV)
NCN	1.94	−0.896	1.04
TiO_2	3.24	−0.534	2.70
$NCNT_5$	2.68	−0.942	1.73

compared to NCN and TiO_2. The results show that $NCNT_5$ S-scheme heterojunctions are more easily activated by visible light, resulting in extra photo-generated electrons,[68,69] which indicates improved photocatalytic hydrogen production by powerful visible-light $NCNT_5$. These findings suggest that NCN's $NCNT_5$ could improve charge separation and activity, thus enhancing photocurrent responses.

As a result, it is not surprising that the $NCNT_5$ sample exhibited more excellent photocatalytic activity than bare NCN and TiO_2 due to its greater separation efficiency. Fig. 6b depicts the Nyquist plots of pure NCN, TiO_2, and $NCNT_5$. The diameter of the semicircle arranged on an EIS plot agrees with the electron-transfer resistance in a sample.[70–72] Because $NCNT_5$ has a smaller arc radius than NCN and TiO_2, the composite has lower energy transference resistance. Forming the S-scheme heterojunction significantly improves the movement and separation efficiency in the $NCNT_5$ sample. These data show that $NCNT_5$ composites outperform single components in electron–hole transportation and partition.

In Fig. 6c, the adequate slopes of the Mott–Schottky plots of the samples revealed their n-type semiconducting nature. As a result, their CB positions can be determined using their plane band capacities, which are determined by the (x) values of their Mott–Schottky curves' linear regions. Thus, the generalized CB positions of NCN, TiO_2, and $NCNT_5$ samples were −0.89, −0.53, and −0.94 V (*vs.* Ag/AgCl).[73] The band gaps of NCN (1.94 eV), TiO_2 (3.24 eV), and $NCNT_5$ (2.68 eV) were used to calculate their VB positions, which were 1.04, 2.70, and 1.73 V, respectively, as shown in Table 3.

3.6. Photocatalytic hydrogen production activity

The photocatalytic activity of $NCNT_x$ composites was further validated using an H_2-evolution experiment. According to the controlled experiments, neither the absence of a photocatalyst nor the non-appearance of light irradiation produced measurable H_2. Photocatalytic H_2 production and the consistency of the prepared photocatalysts were tested for triethanolamine 10% as the sacrificial electron donor under sunlight. Fig. 7a displays the hydrogen production amount and maximum H_2 production rate of the g-CN samples. The TiO_2 sample had a lower H_2-evolution rate of (31.2 μmol g^{-1}), which could be the reason for the small surface area and fewer active photocatalytic sites. Close examination of the effects of g-CN precursors and their bonding with the $NCNT_x$ revealed that the order of H_2

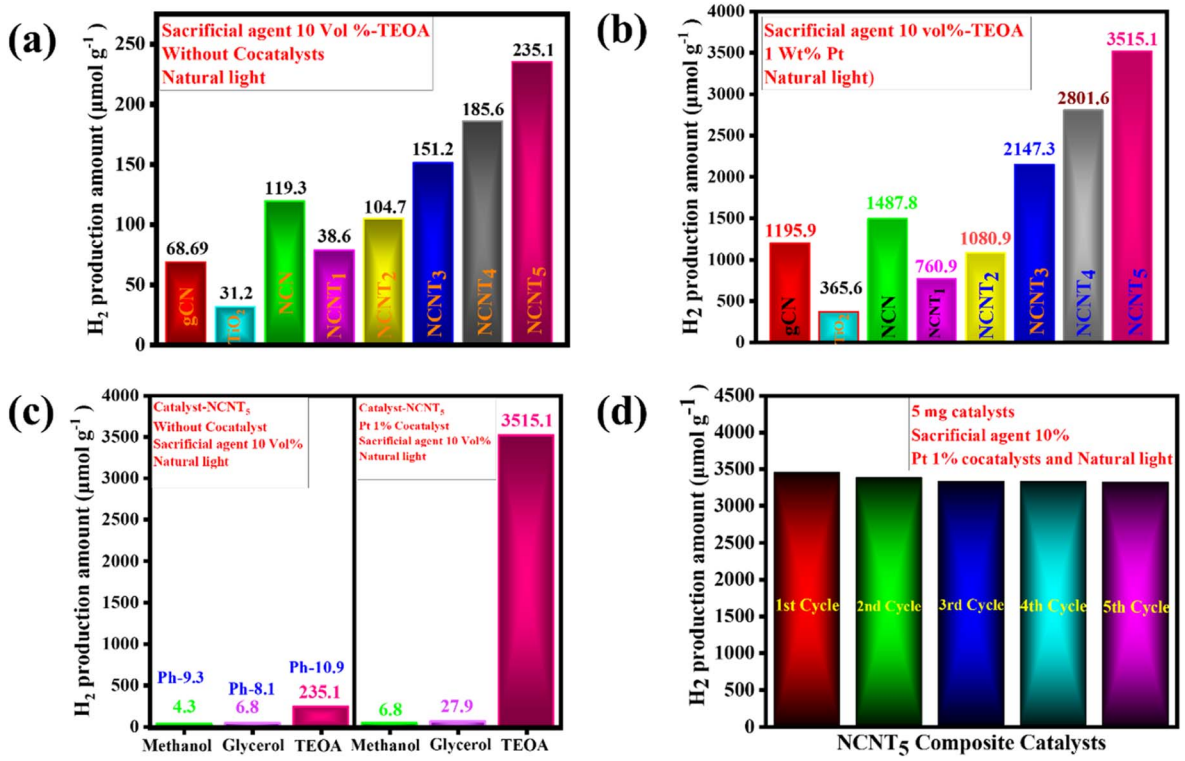

Fig. 7 H_2 generation activity in the photocatalysts. Exposure of sunlight to 5 mg catalyst, TEOA 10 vol% (a), exposure of sunlight to 5 mg catalyst, Pt (1 wt%) cocatalyst, TEOA 10 vol% (b), exposure of sunlight with the 10 vol% sacrificial agents, with and without cocatalyst, and 5 mg catalyst (c), and the re-usability of the $NCNT_5$ catalyst after exposure, 5 mg catalyst, Pt (1 wt%) cocatalyst, TEOA 10 vol% (d).

evolution under solar light was g-CN (68.69 μmol g^{-1}), NCN (119.3 μmol g^{-1}), $NCNT_1$ (38.6 μmol g^{-1}), $NCNT_2$ (104.7 μmol g^{-1}), $NCNT_3$ (151.2 μmol g^{-1}), $NCNT_4$ (185.6 μmol g^{-1}), $NCNT_5$ (235.1 μmol g^{-1}) Fig. 4a.

With cocatalysts, the amount of hydrogen production was similarly determined under natural sunlight. The Pt 1 wt% cocatalyst was used with 10% triethanolamine to improve the photocatalyst activity, and the activity of $NCNT_x$ towards H_2 production was investigated. Compared to g-CN, NCN, TiO_2, and $NCNT_x$ without a cocatalyst, the photocatalytic hydrogen evolution rate improved with a cocatalyst. The bare TiO_2 had a poor photocatalytic H_2 production rate of (365.6 μmol g^{-1}), possibly because of the rapid recombination of electron–hole pairs. After 3 hours of reaction, the amount of hydrogen produced by these bare g-CN catalysts was close to 1195.9 μmol g^{-1}. Fig. 7b demonstrates a significant shift in photocatalyst effectiveness to H_2 evolution in the order of NCN (1487.8 μmol g^{-1}), $NCNT_1$ (760.9 μmol g^{-1}), $NCNT_2$ (1080.9 μmol g^{-1}), $NCNT_3$ (2147.3 μmol g^{-1}), $NCNT_4$ (2801.6 μmol g^{-1}), and $NCNT_5$ (3515.1 μmol g^{-1}). Related to the new photocatalysts, g-CN, NCN, TiO_2, and $NCNT_x$, with 1% Pt as a cocatalyst, produced significantly more hydrogen. The increased output could be attributed to the short band gap, more excellent sunlight absorption, and charge carrier division caused by the suitable band orientation of g-CN, NCN, TiO_2, and $NCNT_x$.

Fig. 7c depicts several sacrificial agents, such as methanol, glycerol, and triethanolamine, resulting from the photocatalytic H_2 production of the NCNT5 composite. TEOA (235.1 μmol g^{-1}), methanol (4.3 μmol g^{-1}), and glycerol (6.8 μmol g^{-1}) had the highest H_2 production rates for the $NCNT_5$ composite without cocatalysts. Hydrogen production rates for Pt 1% cocatalysts with $NCNT_5$ composite were as follows: TEOA (3515.1 μmol g^{-1}), glycerol (27.9 μmol g^{-1}), methanol (6.8 μmol g^{-1}). Furthermore, as shown in Fig. 7c, a system's primary pH significantly impacts photocatalytic activity. The rate of hydrogen evolution was most significant at pH = 10.9 (235.1 μmol g^{-1}) and was insignificant in acidic pH. In an acidic environment, triethanolamine is protonated, preventing the loss of H^+ from $TEOA^+$. In a virtual environment, H_2 formation from water is suppressed due to an increase in repulsive force and a decrease in the ability of TEOA to be adsorbed on the photocatalyst surface.[74]

Fig. 7d displays the amount of H_2-evolution for the $NCNT_5$ composite over five cycles. After each test, a sacrificial agent, triethanolamine, was filled, and the entire hydrogen production activity was re-evaluated. The quantity of H_2 produced was reserved for up to five cycles, and the cycling experiment demonstrated stability. As a result, the $NCNT_5$ composite could be a promising material for improving photocatalysis efficiency.

The maximum H_2 production activity completed on a photocatalyst with a cocatalyst created on $NCNT_5$ is shown in Table 4. The improved photocatalytic activity of $NCNT_5$ can be attributed to forming an active, S-scheme heterojunction between NCN and TiO_2 and the bond of high electron mobility (Pt) to the TiO_2 surface. Furthermore, as a control experiment, photocatalytic H_2 production activity was carried out using various sacrificial agents such as methanol, glycerol, and TEOA. The rates of H_2 production completed with methanol, glycerol, and triethanolamine were 6.8, 27.9, and 3515.1 μmol g^{-1} for 3 hours, respectively.

3.7. Possible photocatalytic reaction mechanism on the $NCNT_x$ S-scheme heterojunction

Based on the analysis above, it was proposed that a photocatalytic mechanism may enhance catalytic capacity. A traditional type-II heterojunction mechanism was first assumed for the composite (Fig. 8 a). TiO_2 and NCN photo-induced electrons (e^-) migrate from the VB to CB under the influence of visible light, leaving holes in the VB (h^+). A more negative CB of NCN (−0.89 eV) than TiO_2 (−0.53 eV) caused (e^-) in the CB of NCN to migrate to TiO_2; the TiO_2 had a more positive VB (2.70 eV) than NCN (1.04 eV), and (h^+) in the VB of TiO_2 migrated to the VB of NCN.[83,84] A more practical S-scheme heterojunction was proposed in Fig. 8b in response to the earlier analysis and report based on the XPS and EPR characteristics.[85] NCN operates as a reduction semiconductor with a greater Fermi level in the NCN/TiO_2 S-scheme heterojunction,[86] whereas TiO_2 acts as an oxidized semiconductor with lower Fermi levels.[87] As well as determining Fermi levels (E_f), we obtained band structures of samples using Mott–Schottky plots. A shift from −0.53 to −0.89 V was observed after NCN/TiO_2 treatment, as shown in Fig. 8b. Water reduction potential and E_f levels are represented by the flat band potential.[88] A heterojunction formed between TiO_2 and NCN initiated spontaneous electron transport to TiO_2 before the equilibrium of the Fermi level. According to the XPS analysis, an internal electric field (IEF) formed at the interface between TiO_2 and NCN. TiO_2 and NCN semiconductors react when visible light irradiates their internal electric fields, in

Table 4 The similarity of the photocatalytic activity in H_2 production from g-C_3N_5 and the TiO_2-based photocatalyst

Composite photocatalysts	Cocatalyst	Sacrificial agent	Light source	H_2 production (μmol g^{-1})	Year	Ref.
g-C_3N_5	—	Triethanolamine	300 W Xe lamp	28.97	2020	75
g-C_3N_5/poly(triazine imide)	Pt	Triethanolamine	Natural light	2326.8	2022	76
g-C_3N_4/TiO_2	Pt	Triethanolamine	300 W Xe	329	2016	77
S-doped g-C_3N_4	—	Triethanolamine	450 W Xe	986	2017	78
C_3N_5/CdS	—	Na_2S and Na_2SO_3	300 W Xe	7860	2023	79
$LaCoO_3$/C_3N_5	—	Methanol	300 W Xe	956.11	2022	80
P-doped C_3N_5	Pt	Triethanolamine	300 W Xe	318	2020	81
S-doped C_3N_5	Pt	Triethanolamine	450 W Xe	486	2023	82
N doped g-C_3N_5/TiO_2	Pt	Triethanolamine	Natural light	3515.1	2022	This work

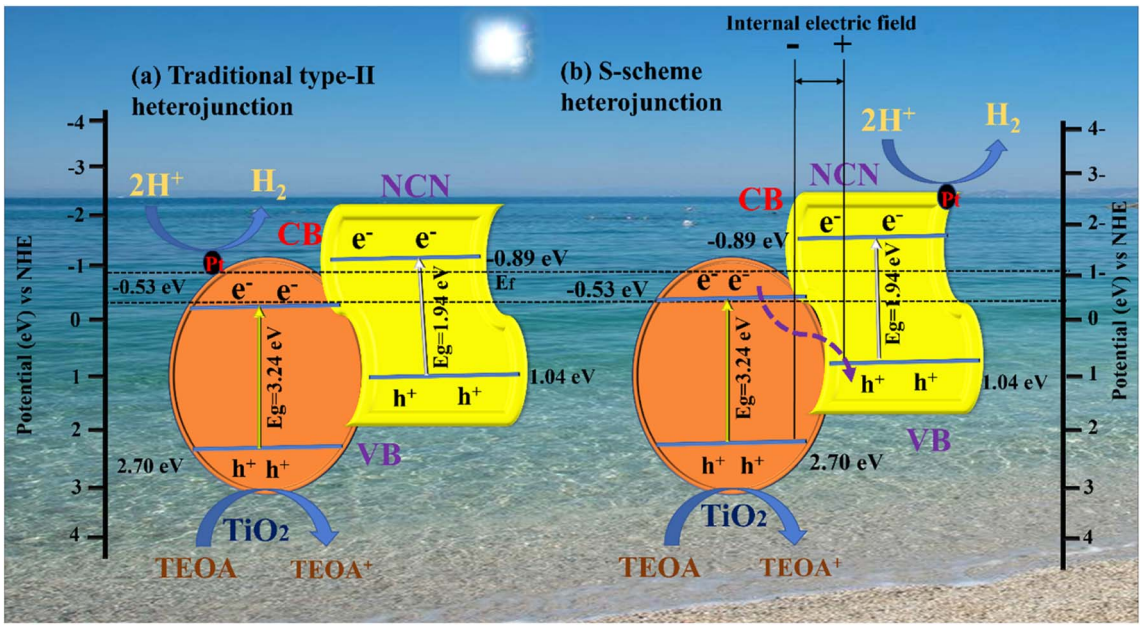

Fig. 8 Proposed charge separation and transfer mechanisms of the NCNT$_x$ photocatalyst: (a) traditional type-II heterojunction, (b) S-scheme heterojunction.

which the electrons in the CB of TiO_2 migrate to the VB of NCN, becoming more effective electrons while retaining more CB holes from NCN and holes VB from TiO_2 (eqn (1)). With the assistance of Pt (eqn (2)), the electrons in the CB of NCN combined with (H^+) to produce H_2. The oxidation reaction was carried out by the holes that accumulated in TiO_2 (eqn (3)). As a result of electron separation, the CB donates its electrons to an electron acceptor such as H^+ (eqn (4)). H_2 is formed as a result of this donation. The surface adsorbed (Pt^{2+}) was subsequently reduced by electrons deposited in the CB of TiO_2, and the newly designed Pt was deposited on the TiO_2 surface as an efficient cocatalyst for Hydrogen evolution.[89,90] This composite enhances photocatalytic activity by suppressing the recombination of photogenerated electron–hole pairs, and broadening the light absorption range. In addition, it can increase the efficiency of electron–hole separation. As a result, the photocatalytic activity of the N-doped g-C_3N_5/TiO_2 composite with Pt as cocatalysts is significantly improved.

$$NCN/TiO_2 + h\nu \rightarrow h^+ + e^- \quad (1)$$

$$H_2O + h^+ \rightarrow H^+ + {}^{\cdot}OH \quad (2)$$

$$TEOA + h^+ \rightarrow TEOA^+ \quad (3)$$

$$e^- + H^+ \rightarrow H_2 \quad (4)$$

3.8. DFT calculations

Two possible doping locations were evaluated in the g-CN structure (named C1 and C2). According to earlier research and DFT calculations, the construction energy of a substitutional nitrogen atom in the C1 position was significantly less than in the C2 site.[22,36] In this study, however, the construction energy of a substitutional N atom in the C2 position was considerably less than in the C1 area. As a result of its lower construction energy, C2 is more actively supportive of N atom doping. Fig. 9a and b depicts the optimized geometric structure (shown by the yellow ball). Hence, it was concluded that some of the C sites in g-C_3N_5 must have had N species replacing the C atoms to produce N–N=N bonds.[91]

Table S3,† the calculated HOMO–LUMO values for g-CN were −5.90 eV (HOMO) and −3.18 eV (LUMO). The inclusion of nitrogen in NCN as compared to g-CN leads to a linear destabilization of the HOMO value (−5.73 eV) and stabilization of the LUMO value (−3.34 eV), resulting in a reduced band gap of 2.34 eV as compared to the g-CN molecule (2.72 eV) Fig. 9c. These analyses revealed that the calculated results demonstrated consistent trends with the experimental values. Furthermore, we employed a combination of hybrid B3LYP, PBE_0, and meta-hybrid M06 and M06-2X functionals to simulate the absorption studies with the 6-31+G* basis set.[92–94] The table revealed a clear linear correlation between the absorption values and the Hartree–Fock values within the functional. The absorption range for both molecules, determined using the M06-2X functional, closely matched the experimentally measured absorption values, falling within the range of 390 nm to 394 nm, while the experimental values ranged from 365 nm to 375 nm (Fig. 9d). A broad absorption band was observed for g-C_3N_5 and nitrogen-doped g-C_3N_5, with absorption edges at 461 and 484 nm (Table S4†), consistent with DFT calculations. The natural transition orbital (NTO) maps further validated the presence of a similar absorption range in both the g-CN and NCN molecules.[95] The NTOs for both the holes and electrons

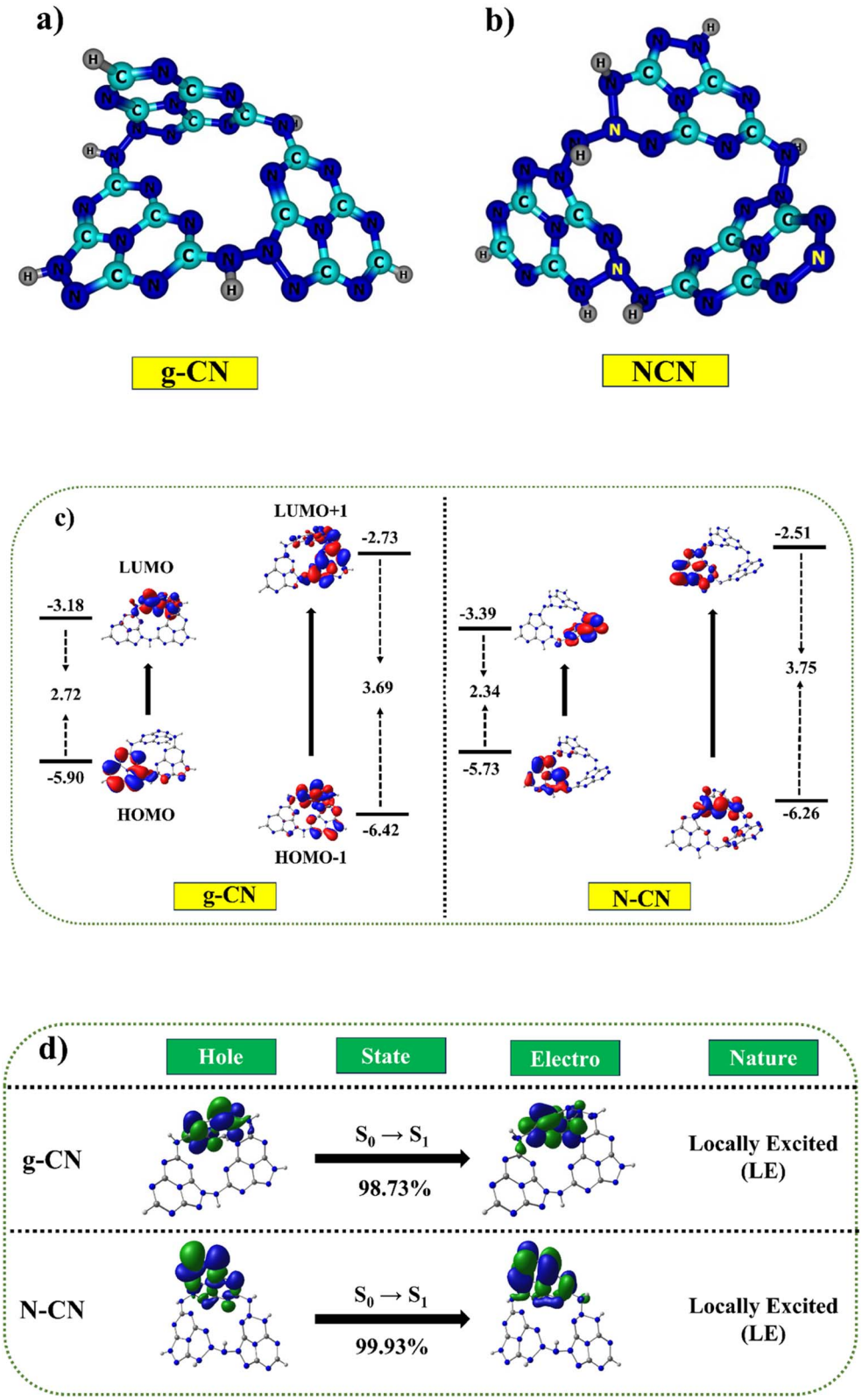

Fig. 9 The probable existing forms of g-C_3N_5 and N-doped g-C_3N_5 (a and b). Correlation diagram for the frontier orbitals (FMOs in eV) of g-CN and NCN trimers (iso-surface value = 0.02 au) (c). Hole-particle NTOs (iso-surface value = 0.02 au.) of g-CN and NCN molecules with excited state transition character (d).

were predominantly localized within the sole monomer units, indicating locally excited characteristics. The calculated energies exhibited a remarkable agreement with the experimentally measured values, highlighting the noteworthy correspondence achieved for the ground and excited state energies using the O3LYP and M06-2X functionals, respectively.

4. Conclusion

We have reported a new photocatalyst using the N-doped g-C_3N_5/TiO_2 composite as an effective photocatalyst for visible-light-assisted photocatalytic hydrogen production. The XRD and XPS results have demonstrated fruitful nitrogen doping on the C_2 site of g-C_3N_5. The DFT calculations, PL, and XPS results show that the nitrogen doping occurred on the C2 site of g-C_3N_5; as indicated by the fluctuation in charge density, constant PEC, and PL spectra, $NCNT_x$ exhibits excellent photo-generated carrier separation and charge transfer, enhancing photocatalytic activity. Photocurrent and EIS analysis predicted the S-scheme heterojunction mechanism to explain the electron process flow in composites, especially in the presence of light. The efficacy of H_2 production on the nitrogen-doped g-C_3N_5/TiO_2 for 3 hours (3515.1 μmol g^{-1}) without a co-catalyst is about three times that of N-doped g-C_3N_5. The efficacy of the nitrogen-doped g-C_3N_5/TiO_2 catalyst with Pt as the cocatalyst significantly showed a ten-fold increase in performance as compared to the N-doped g-C_3N_5/TiO_2 without cocatalyst. This work highlights the photocatalytic reaction of the N-doped g-C_3N_5/TiO_2 composite with Pt as a cocatalyst. It demonstrates a promising strategy for the efficient production of hydrogen through the S-scheme mechanism.

Conflicts of interest

The authors declare that they have no known competing financial interests or personal relationships that could have appeared to influence the work reported in this paper.

Acknowledgements

K. Saravanan acknowledges financial support from the University Research Fellowship (URF) SRM Institute of Science and Technology, Tamil Nadu 603 203, India. The authors gratefully acknowledge the XRD, HR-TEM facilities at SRMIST set up with support from MNRE (project no. 31/03/2014-15/PVSE-R&D), Government of India. We acknowledge NRC, SRM Institute of Science and Technology, for providing the FE-SEM facility. The authors acknowledge SRM Institute of Science and Technology for providing the UV-visible DRS facility. Finally, the authors are grateful for the SRM Research Institute of Science and Technology facilities.

References

1 Y. Li, S. Zhu, Y. Liang, Z. Li, S. Wu, C. Chang, S. Luo and Z. Cui, *Mater. Des.*, 2020, **196**, 109191.
2 X. Zhai, P. Zhang, C. Liu, T. Bai, W. Li, L. Dai and W. Liu, *Chem. Commun.*, 2012, **48**, 7955–7957.
3 Y. Wang, X. Liu, C. Zheng, Y. Li, S. Jia, Z. Li and Y. Zhao, *Adv. Sci.*, 2018, **5**, 1700844.
4 H. Li, C. Jin, Z. Wang, Y. Liu, P. Wang, Z. Zheng, M. H. Whangbo, L. Kou, Y. Li, Y. Dai and B. Huang, *Chem. Eng. J.*, 2019, **369**, 263–271.
5 H. Li, C. Jin, Z. Wang, Y. Liu, P. Wang, Z. Zheng, M. H. Whangbo, L. Kou, Y. Li, Y. Dai and B. Huang, *Chem. Eng. J.*, 2019, **369**, 263–271.
6 Q. Dong, Y. Fang, Y. Shao, P. Mulligan, J. Qiu, L. Cao and J. Huang, *Science*, 2015, **347**, 967–970.
7 S. Otsuka-Yao-Matsuo, T. Omata and M. Yoshimura, *J. Alloys Compd.*, 2004, **376**, 262–267.
8 L. Liang, L. Shi, F. Wang, H. Wang and W. Qi, *Sustainable Energy Fuels*, 2020, **4**, 5179–5187.
9 X. She, L. Liu, H. Ji, Z. Mo, Y. Li, L. Huang, D. Du, H. Xu and H. Li, *Appl. Catal., B*, 2016, **187**, 144–153.
10 J. Xu and M. Antonietti, *J. Am. Chem. Soc.*, 2017, **139**, 6026–6029.
11 X. Bai, L. Wang, R. Zong and Y. Zhu, *J. Phys. Chem. C*, 2013, **117**, 9952–9961.
12 W. J. Jo, J. W. Jang, K. J. Kong, H. J. Kang, J. Y. Kim, H. Jun, K. P. S. Parmar and J. S. Lee, *Angew. Chem., Int. Ed.*, 2012, **51**, 3147–3151.
13 Y. Liu, S. Wu, J. Liu, S. Xie and Y. Liu, *RSC Adv.*, 2021, **11**, 4810–4817.
14 H. Zhang, F. Liu, H. Wu, X. Cao, J. Sun and W. Lei, *RSC Adv.*, 2017, **7**, 40327–40333.
15 N. Tian, Y. Zhang, X. Li, K. Xiao, X. Du, F. Dong, G. I. N. Waterhouse, T. Zhang and H. Huang, *Nano Energy*, 2017, **38**, 72–81.
16 F. Ling, W. Li and L. Ye, *Appl. Surf. Sci.*, 2019, **473**, 386–392.
17 C. Hu, M. S. Wang, C. H. Chen, Y. R. Chen, P. H. Huang and K. L. Tung, *J. Membr. Sci.*, 2019, **580**, 1–11.
18 L. Liang, L. Shi, F. Wang, H. Wang, P. Yan, Y. Cong, L. Yao, Z. Yang and W. Qi, *Appl. Catal., A*, 2020, **599**, 117618.
19 L. T. Huynh, S. B. Eger, J. D. S. Walker, J. R. Hayes, M. W. Gaultois and A. P. Grosvenor, *Solid State Sci.*, 2012, **14**, 761–767.
20 D. H. Park, K. S. Lakhi, K. Ramadass, M. K. Kim, S. N. Talapaneni, S. Joseph, U. Ravon, K. Al-Bahily and A. Vinu, *Chem.–Eur. J.*, 2017, **23**, 10753–10757.
21 F. He, Z. Wang, Y. Li, S. Peng and B. Liu, *Appl. Catal., B*, 2020, **269**, 118828.
22 G. P. Mane, S. N. Talapaneni, K. S. Lakhi, H. Ilbeygi, U. Ravon, K. Al-Bahily, T. Mori, D. Park and A. Vinu, *Angew. Chem.*, 2017, **129**, 8601–8605.
23 W. Wang, M. Chen, D. Huang, G. Zeng, C. Zhang, C. Lai, C. Zhou, Y. Yang, M. Cheng, L. Hu, W. Xiong, Z. Li and Z. Wang, *Composites, Part B*, 2019, **172**, 704–723.
24 Y. Zhou, L. Zhang, W. Huang, Q. Kong, X. Fan, M. Wang and J. Shi, *Carbon*, 2016, **99**, 111–117.
25 B. Luo, R. Song, J. Geng, D. Jing and Y. Zhang, *Appl. Catal., B*, 2018, **238**, 294–301.
26 C. Jia, L. Yang, Y. Zhang, X. Zhang, K. Xiao, J. Xu and J. Liu, *ACS Appl. Mater. Interfaces*, 2020, **12**, 53571–53591.

27 T. Liu, W. Chen, Y. Hua and X. Liu, *Appl. Surf. Sci.*, 2017, **392**, 616–623.
28 C. Hu, Y. R. Lin and H. C. Yang, *ChemSusChem*, 2019, **12**, 1794–1806.
29 C. Zhao, Q. Li, Y. Xie, L. Zhang, X. Xiao, D. Wang, Y. Jiao, C. A. Hurd Price, B. Jiang and J. Liu, *J. Mater. Chem. A*, 2020, **8**, 305–312.
30 A. Thomas, A. Fischer, F. Goettmann, M. Antonietti, J. O. Müller, R. Schlögl and J. M. Carlsson, *J. Mater. Chem.*, 2008, **18**, 4893–4908.
31 J. Ran, T. Y. Ma, G. Gao, X. W. Du and S. Z. Qiao, *Energy Environ. Sci.*, 2015, **8**, 3708–3717.
32 Z. F. Huang, J. Song, L. Pan, Z. Wang, X. Zhang, J. J. Zou, W. Mi, X. Zhang and L. Wang, *Nano Energy*, 2015, **12**, 646–656.
33 M. Xiao, B. Luo, S. Wang and L. Wang, *J. Energy Chem.*, 2018, **27**, 1111–1123.
34 L. Huang, Z. Liu, W. Chen, D. Cao and A. Zheng, *J. Mater. Chem. A*, 2018, **6**, 7168–7174.
35 Y. Zhu, Y. Feng, S. Chen, M. Ding and J. Yao, *J. Mater. Chem. A*, 2020, **8**, 25626–25648.
36 A. Akbarzadeh, Y. Khazani, S. Khaloo and M. Ghalkhani, *Research Square*, 2022, 1–21.
37 M. Li, Q. Lu, M. Liu, P. Yin, C. Wu, H. Li, Y. Zhang and S. Yao, *ACS Appl. Mater. Interfaces*, 2020, **12**, 38266–38274.
38 D. Zhu and Q. Zhou, *Appl. Catal., B*, 2021, **281**, 119474.
39 S. Vadivel, S. Hariganesh, B. Paul, S. Rajendran, A. Habibi-Yangjeh, D. Maruthamani and M. Kumaravel, *Chem. Phys. Lett.*, 2020, **738**, 136862.
40 I. Y. Kim, S. Kim, X. Jin, S. Premkumar, G. Chandra, N. S. Lee, G. P. Mane, S. J. Hwang, S. Umapathy and A. Vinu, *Angew. Chem., Int. Ed.*, 2018, **57**, 17135–17140.
41 S. Hu, L. Ma, J. You, F. Li, Z. Fan, G. Lu, D. Liu and J. Gui, *Appl. Surf. Sci.*, 2014, **311**, 164–171.
42 Q. Wang, G. Zhang, W. Xing, Z. Pan, D. Zheng, S. Wang, Y. Hou and X. Wang, *Angew. Chem., Int. Ed.*, 2023, **62**, e202307930.
43 Y. Wang, R. Shi, J. Lin and Y. Zhu, *Energy Environ. Sci.*, 2011, **4**, 2922–2929.
44 Q. Guo, Y. Xie, X. Wang, S. Zhang, T. Hou and S. Lv, *Chem. Commun.*, 2004, **4**, 26–27.
45 S. Obregón and G. Colón, *Appl. Catal., B*, 2014, **144**, 775–782.
46 G. Li, G. Zeng, Z. Chen, J. Hong, X. Ji, Z. Lan, X. Tan, M. Li, X. Hu and C. Tang, *Nanomaterials*, 2022, **12**, 2701.
47 L. Wang, M. Li, Q. Zhang, F. Li and L. Xu, *Inorg. Chem. Front.*, 2021, **8**, 3566–3575.
48 F. Xu, B. Zhu, B. Cheng, J. Yu and J. Xu, *Adv. Opt. Mater.*, 2018, **6**, 1800911.
49 F. He, G. Chen, Y. Yu, Y. Zhou, Y. Zheng and S. Hao, *Chem. Commun.*, 2015, **51**, 425–427.
50 W. Zhou, L. Lin, W. Wang, L. Zhang, Q. Wu, J. Li and L. Guo, *J. Phys. Chem. C*, 2011, **115**, 7126–7133.
51 R. Hao, G. Wang, C. Jiang, H. Tang and Q. Xu, *Appl. Surf. Sci.*, 2017, **411**, 400–410.
52 S. Yang, Y. Gong, J. Zhang, L. Zhan, L. Ma, Z. Fang, R. Vajtai, X. Wang and P. M. Ajayan, *Adv. Mater.*, 2013, **25**, 2452–2456.
53 D. Zhu and Q. Zhou, *Appl. Catal., B*, 2021, **281**, 1194.
54 W. Ding, Z. Wei, S. Chen, X. Qi, T. Yang, J. Hu, D. Wang, L. J. Wan, S. F. Alvi and L. Li, *Angew. Chem., Int. Ed.*, 2013, **52**, 11755–11759.
55 Y. Zhou, L. Zhang, W. Huang, Q. Kong, X. Fan, M. Wang and J. Shi, *Carbon*, 2016, **99**, 111–117.
56 Y. Wang, X. Cui, Y. Li, L. Chen, H. Chen, L. Zhang and J. Shi, *Carbon*, 2014, **68**, 232–239.
57 J. Li, L. Zhao, S. Wang, J. Li, G. Wang and J. Wang, *Appl. Surf. Sci.*, 2020, **515**, 145922.
58 T. Liu, G. Yang, W. Wang, C. Wang, M. Wang, X. Sun, P. Xu and J. Zhang, *Environ. Res.*, 2020, **188**, 109741.
59 X. Shi, M. Fujitsuka, Z. Lou, P. Zhang and T. Majima, *J. Mater. Chem. A*, 2017, **5**, 9671–9681.
60 P. Kumar, E. Vahidzadeh, U. K. Thakur, P. Kar, K. M. Alam, A. Goswami, N. Mahdi, K. Cui, G. M. Bernard, V. K. Michaelis and K. Shankar, *J. Am. Chem. Soc.*, 2019, **141**, 5415–5436.
61 Y. Gong, H. Li, C. Jiao, Q. Xu, X. Xu, X. Zhang, Y. Liu, Z. Dai, X. Y. Liu, W. Chen, L. Liu and D. Zhan, *Appl. Catal., B*, 2019, **250**, 63–70.
62 H. Wang, M. Li, Q. Lu, Y. Cen, Y. Zhang and S. Yao, *ACS Sustain. Chem. Eng.*, 2019, **7**, 625–631.
63 S. Vadivel, S. Hariganesh, B. Paul, G. Mamba and P. Puviarasu, *Colloids Surf., A*, 2020, **592**, 124583.
64 A. B. Djurišić, Y. He and A. M. C. Ng, *APL Mater.*, 2020, **8**, 030903.
65 Y. Chen, C. Liu, S. Guo, T. Mu, L. Wei and Y. Lu, *Green Energy Environ.*, 2022, **7**, 394–410.
66 R. Tao, X. Li, X. Li, C. Shao and Y. Liu, *Nanoscale*, 2020, **12**, 8320–8329.
67 J. Li, M. Li, H. Li and Z. Jin, *J. Mater. Chem. C*, 2022, **10**, 2181–2193.
68 C. Lv, X. Lan, F. Li, L. Wang, L. Xiao, C. Wang, J. Shi and S. Yu, *Catal. Sci. Technol.*, 2020, **10**, 690–699.
69 F. Amano, M. Nakata, A. Yamamoto and T. Tanaka, *Catal. Sci. Technol.*, 2016, **6**, 5693–5699.
70 V. D. Dang, J. Adorna, T. Annadurai, T. A. N. Bui, H. L. Tran, L. Y. Lin and R. A. Doong, *Chem. Eng. J.*, 2021, **422**, 130103.
71 A. Babu Ganganboina, M. Dung Nguyen, T. Hien Luong Nguyen, E. Prasetyo Kuncoro and R. A. Doong, *Chem. Eng. J.*, 2021, **425**, 131520.
72 X. Zhang, L. Shi and Y. Zhang, *J. Taiwan Inst. Chem. Eng.*, 2022, **132**, 104111.
73 H. Zhao, H. Yu, X. Quan, S. Chen, H. Zhao and H. Wang, *RSC Adv.*, 2014, **4**, 624–628.
74 A. Rajan and B. Neppolian, *Appl. Mater. Today*, 2022, **28**, 101524.
75 T. Liu, G. Yang, W. Wang, C. Wang, M. Wang, X. Sun, P. Xu and J. Zhang, *Environ. Res.*, 2020, **188**, 109741.
76 J. Zhang, H. Tao, S. Wu, J. Yang and M. Zhu, *Appl. Catal., B*, 2021, **296**, 120372.
77 J. Ma, X. Tan, T. Yu and X. Li, *Int. J. Hydrogen Energy*, 2016, **41**, 3877–3887.
78 J. S. Kim, J. W. Oh and S. I. Woo, *Int. J. Hydrogen Energy*, 2017, **42**, 5485–5495.
79 X. Wang, K. Wu, W. Cao, K. Rui, W. Wang, R. Zhu, J. Zhu and Z. Yan, *Adv. Mater. Interfaces*, 2023, **10**, 2201627.

80 R. Wang, K. Zhang, X. Zhong and F. Jiang, *RSC Adv.*, 2022, **12**, 24026–24036.
81 Q. Lin, Z. Li, T. Lin, B. Li, X. Liao, H. Yu and C. Yu, *Chin. J. Chem. Eng.*, 2020, **28**, 2677–2688.
82 X. Guan, M. Fawaz, R. Sarkar, C. H. Lin, Z. Li, Z. Lei, P. D. Nithinraj, P. Kumar, X. Zhang, J. H. Yang, L. Hu, T. Wu, S. Chakraborty, J. Yi and A. Vinu, *J. Mater. Chem. A*, 2023, **11**, 12837–12845.
83 S. Li, M. Cai, Y. Liu, J. Zhang, C. Wang, S. Zang, Y. Li, P. Zhang and X. Li, *Inorg. Chem. Front.*, 2022, **9**, 2479–2497.
84 J. Bai, R. Shen, K. Zhou, Z. Jiang, P. Zhang and X. Li, *Chin. J. Catal.*, 2022, **43**, 359–369.
85 B. Li, B. Zhang, Y. Zhang, M. Zhang, W. Huang, C. Yu, J. Sun, J. Feng, S. Dong and J. Sun, *Int. J. Hydrogen Energy*, 2021, **46**, 32413–32424.
86 J. Fu, Q. Xu, J. Low, C. Jiang and J. Yu, *Appl. Catal., B*, 2019, **243**, 556–565.
87 Z. Wang, Y. Chen, L. Zhang, B. Cheng, J. Yu and J. Fan, *J. Mater. Sci. Technol.*, 2020, **56**, 143–150.
88 L. Wang, C. S. Tsang, W. Liu, X. Zhang, K. Zhang, E. Ha, W. M. Kwok, J. H. Park, L. Y. Suk Lee and K. Y. Wong, *J. Mater. Chem. A*, 2019, **7**, 221–227.
89 J. T. Lee, Y. J. Chen, E. C. Su and M. Y. Wey, *Int. J. Hydrogen Energy*, 2019, **44**, 21413–21423.
90 J. Zhang, L. Wang, M. Mousavi, J. B. Ghasemi and J. Yu, *Jiegou Huaxue*, 2022, **41**, 2206003–2206005.
91 C. Hu, Y. H. Lin, M. Yoshida and S. Ashimura, *ACS Appl. Mater. Interfaces*, 2021, **13**, 24907–24915.
92 C. Adamo and V. Barone, *J. Chem. Phys.*, 1999, **110**, 6158–6170.
93 R. Valero, R. Costa, I. d. P. R. Moreira, D. G. Truhlar and F. Illas, *J. Chem. Phys.*, 2008, **128**, 114103.
94 J. Tirado-Rives and W. L. Jorgensen, *J. Chem. Theory Comput.*, 2008, **4**, 297–306.
95 R. L. Martin, *J. Chem. Phys.*, 2003, **118**, 4775–4777.